Moiré-Induced Vibrational Coupling in Double-Walled Carbon Nanotubes

Georgy Gordeev, Sören Wasserroth, Han Li, Benjamin Flavel, and Stephanie Reich

ABSTRACT: Moiré patterns are additional, long range periodicities in twisted crystalline bilayers. They are known to fundamentally change the electronic states of the layers, but similar effects on their mechanical and vibrational properties have not been discussed so far. Here we show that the moiré potential shifts the radial breathing mode in double walled carbon nanotubes (DWCNTs). The change in frequency is expected to be proportional to the shift in optical transition energies, which are induced by the moiré patterns. To verify our model, we performed resonance Raman scattering on purified and sorted semiconducting DWCNTs. We find that the radial breathing mode shifts up to 14 cm^{-1} higher in energy followed by displacement of optical transition energies of up to 200 meV to lower energies, in comparison to the single walled tubes. We show how to identify the strong coupling condition in DWCNTs from their phonon frequencies and construct a Kataura plot to aid their future experimental assignment.

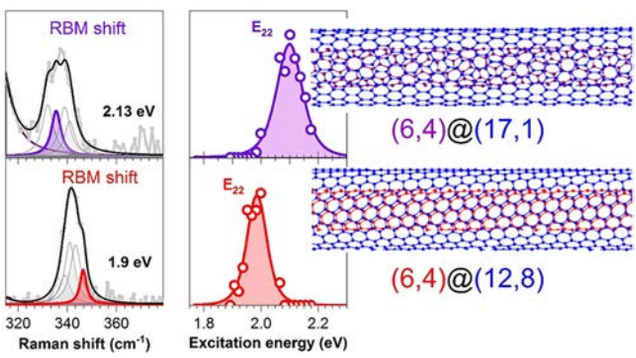

KEYWORDS: *Double walled nanotubes, moiré patterns, electromechanical coupling, Kataura plot, strong coupling, resonance Raman*

INTRODUCTION

Moiré patterns arise from the overlap of two displaced and identical crystalline lattices;[1] they have been shown to drastically affect the electronic properties of two dimensional materials. For example, graphene bilayers with small twist angles show correlated electronic behavior with insulating and superconducting phases[2] and additional van Hove singularities emerge for larger angles.[3] In transition metal dichalcogenides moiré patterns may reconstruct the lattice, resulting in piezoelectric domains.[4] If two chemically different layers are combined, interlayer excitons form where one layer contains an electron and the other layer a hole. The lifetime of these quasi particles depends on the twist angle and moiré structure.[5]

Moiré patterns in one dimensional (1D) systems[6] have received less attention than their two dimensional counterparts, although once they are formed, they will be extremely stable and the 1D confinement introduces an additional degree of freedom for manipulating states.[7−9] Double walled carbon nanotubes (DWCNTs)[10] have distinct moiré patterns that arise from the two concentrically aligned single walled carbon nanotubes with different twists along their axis.[7] Depending on the chirality of the two tubes, the band gap shrinks due to the moiré interaction[8,9] or insulating flat bands are expected,[7] very similar to those found in bilayer graphene.[2] The first challenge in the study of DWCNTs is that there are many possible structures and combinations that are associated with different electronic properties. Nanotube properties depend on diameter, chiral angle, and handedness, which are all determined by their (n_1,n_2) chirality.[11,12] Single walled nanotubes (SWCNTs) are either metallic (M) or semiconducting (S) depending on their chirality,[11] and this results in four basic configurations of inner@outer nanotubes for DWCNTs: S@S, M@M, M@S, and S@M.[13] Since as grown raw soot usually contains all four types and the wall to wall coupling depends sensitively on their electronic character, structure specific studies on bulk DWCNT samples have been very challenging so far.[14,15] In a recent work we succeeded in separating DWCNTs by their electronic type.[16−18] This now enables the study of their properties and moiré physics in a wide range of DWCNTs.

Despite the key role that moiré effects play in the electronic states, the vibrational degrees of freedom have rarely been examined within moiré physics. Moiré patterns activate phonon modes that fulfill the selection rule of a vanishing wave vector only for the superstructure.[19] The moiré period also affects interlayer spacing and, thereby, indirectly changes the frequencies of the interlayer breathing modes by a few

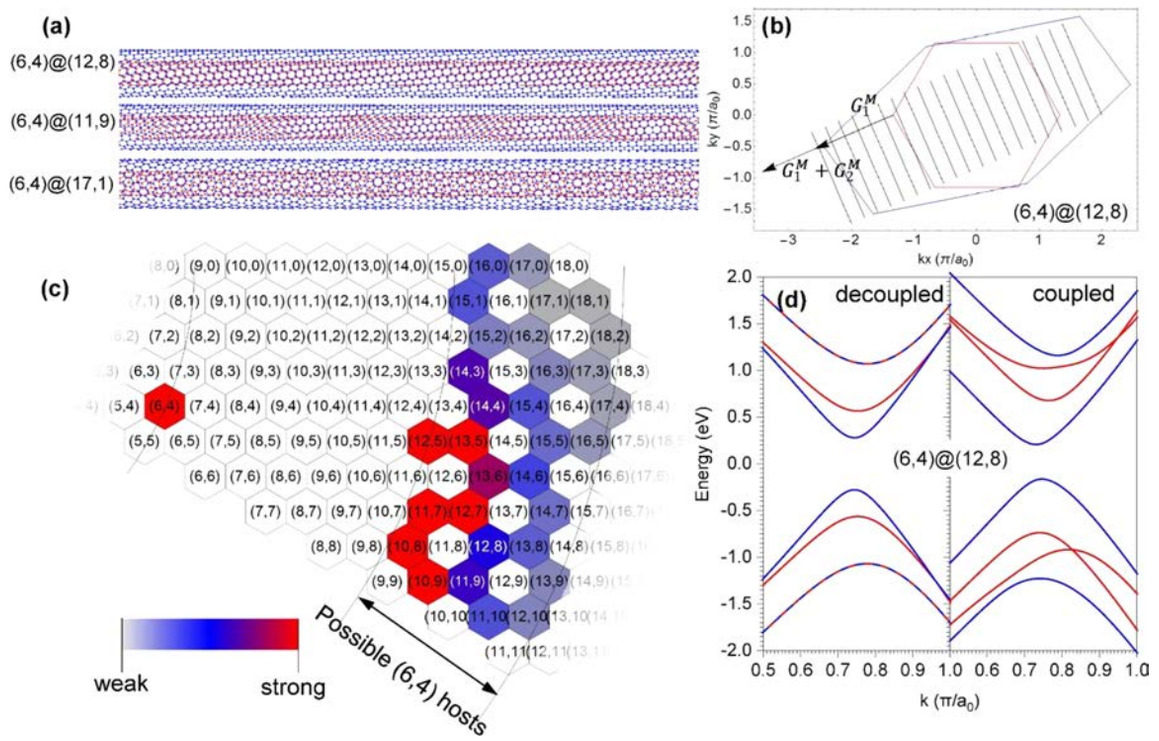

Figure 1. (a) Moiré induced effects in DWCNTs consisting of a (6,4) inner wall (red) with different outer walls (blue). (b) Brillouin zone of the (6,4)@(12,8) DWCNT with moiré vectors included: a_0 = 0.246 nm. The cutting lines are translated into the first BZ. (c) Possible outer wall semiconducting nanotubes for a (6,4) inner wall plotted on a model graphene sheet, where the color indicates the variation in coupling strength from weak (gray) to strong (red). (d) Band structure of a (6,4)@(12,8) nanotube with (right) and without (left) coupling. Bands originating from the (6,4) wall are shown in red and bands of the (12,8) wall in blue.

wavenumbers.[20] The vibrations of DWCNTs, however, have been analyzed from a purely mechanical point of view.[15,21−25] The phonon frequencies of DWCNTs split and shift in comparison to their SWCNT counterparts, which was explained as an effective strain that varies with the wall to wall distance.[21,23,26−28]

In this letter, we show that moiré coupling determines the vibrational properties of DWCNTs. First, a moiré based model is proposed for phonons with radial eigenvectors. The phonon frequencies increase with moiré coupling strength. We confirm the predictions by resonance Raman spectroscopy of S@S enriched DWCNTs. The electronic transition energies become smaller,[7] while the frequencies of radial breathing mode phonons increase, in excellent agreement with our moiré based theory. Finally, we construct a Kataura plot for semiconducting DWCNTs to simplify their future assignment.

RESULTS

The atomic structure of two concentric CNTs and their resulting moiré patterns determine the coupling between the walls of a double walled tube. A DWCNT is characterized by four indices $(n_1^i,n_2^i)@(n_1^o,n_2^o)$ that specify the chiral indices of the inner (i) and outer (o) SWCNT. These indices produce different moiré pattern (see Figure 1a). We will discuss the moiré physics by exemplarily comparing the (6,4)@(12,8) with the (6,4)@(17,1) DWCNTs. One expects the clear superstructure of the (6,4)@(12,8) DWCNT to show stronger interwall coupling in comparison to the (6,4)@(17,1) tube. Indeed, the coupling is stronger for two tubes with similar chiral angles: i.e., for small angles $\varphi\angle(\mathbf{C}^i,\mathbf{C}^o)$ between the two chiral vectors, as is the case for the (6,4)@(12,8) tube.[7] $\mathbf{C}^i = n_1^i\boldsymbol{a}_1 + n_2^i\boldsymbol{a}_2$ corresponds to the inner wall and $\mathbf{C}^o = n_1^o\boldsymbol{a}_1 + n_2^o\boldsymbol{a}_2$ to the outer wall, with $\boldsymbol{a}_1$ and $\boldsymbol{a}_1$ being the basis vectors of graphene.[12] The chiral vectors determine the periodicity of the moiré superstructure.

The coupling strength of a DWCNT can be deduced from its structure in reciprocal space. The Brillouin zone (BZ) of a DWCNT is obtained from the inner tube plus the BZ of the outer tube submitted to two symmetry operations[7] (see Figure 1b). First, we rotate the BZ by φ; this operation P aligns $\mathbf{C}^i$ and $\mathbf{C}^o$. For inner and outer tubes with opposite handedness, 2 times the chiral angle of the outer wall is added to φ. Second, we apply a uniaxial expansion S^{-1}. Its inverse operation S describes a uniaxial contraction of the Bravais lattice along $\mathbf{C}^i$ by $\frac{|\mathbf{C}^i|}{|\mathbf{C}^o|}$, which scales the two chiral vectors to the same length. The reciprocal basis vectors of the resulting moiré super structure are $\boldsymbol{G}_l^M = (\mathbf{1} - S^{-1}P^{-1})\boldsymbol{b}_l$ (l = 1, 2), where $\mathbf{1}$ is the identity matrix and $\boldsymbol{b}_l$ are the reciprocal basis vectors of graphene. In the (6,4)@(12,8) tube $\boldsymbol{G}_1^M$ almost connects the two K points of the BZ of the inner and outer walls (Figure 1b). Such a DWCNT is considered to be in the strong regime of chiral moiré coupling; the same applies if $\boldsymbol{G}_2^M$ or their sum $\sum\boldsymbol{G}_l^M$ connects the two K points. This condition can be expressed geometrically. It requires the two angles $\vartheta\angle(\mathbf{C}^i - \mathbf{C}^o,\boldsymbol{a}_1 + \boldsymbol{a}_2)$ and φ to be close to zero.[7] Figure 1a illustrates this for three different DWCNTs, where φ = 0 and ϑ = 6.6° in the (6,4)@(12,8) tube, φ = 3.3 and ϑ = 0° in the (6,4)@(11,9) tube, and φ = 20.5° and ϑ = 45° in the (6,4)@(17,1) DWCNTs.

The moiré pattern changes the electronic band structure of DWCNTs in comparison to the individual nanotubes. The

Hamiltonian $H_{i,o}$ of a DWCNT can be expressed using the model developed by Koshino et al. as[7]

$$H_{i,o} = \begin{pmatrix} H_i(\boldsymbol{k}) & U^{\dagger} \\ U & H_o(\boldsymbol{k}) \end{pmatrix} \tag{1}$$

where U is the interlayer coupling matrix element and $H_i(\boldsymbol{k})$ and $H_o(\boldsymbol{k})$ are Hamiltonians of the inner and outer walls, respectively. We use the tight binding model of graphene for $H_i(\boldsymbol{k})$, with hopping energy y_c = 2.7 eV.[12,29] $H_o(\boldsymbol{k})$ is obtained from the tight binding Hamiltonian by transforming the vectors connecting neighboring atoms according to $T_u^0 = T_u^i SP$ (see the Supporting Information). The interlayer matrix element is expressed in terms of the moiré vectors as[7]

$$U = u_0(R)\left(\mathbf{1} + \begin{pmatrix} 1 & \omega^{-1} \\ \omega^{1} & 1 \end{pmatrix} e^{I\xi \mathbf{G}_1^M \cdot r} + \begin{pmatrix} 1 & \omega^{1} \\ \omega^{-1} & 1 \end{pmatrix} e^{I\xi(\mathbf{G}_1^M + \mathbf{G}_2^M)\cdot r}\right) \tag{2}$$

where $\omega = \exp(2\pi I\xi/3)$ and $\xi = \pm 1$ denotes time reversal partners. $u_0(R)$ is a coupling amplitude dependent on the interlayer distance. The band structure can be calculated numerically by the zone folding approach. We use eq 1 with the quantization condition around the circumference of $\boldsymbol{k}\cdot\mathbf{C}^i = 2\pi m$, where m enumerates the cutting line (Figure 1b).

The electronic dispersion of the SWCNT becomes perturbed by the formation of a DWCNT. The band structure of the (6,4)@(12,8) nanotube is depicted in Figure 1d. In the uncoupled case, the E_{22} band energies from the inner and outer walls overlap for this particular pair of chiralities. In the coupled case, the positions of the E_{22} electronic bands from the (12,8) outer wall move apart, increasing the second band gap. For the (6,4) inner wall the energies move closer together, reducing the band gap. Figure 1c schematically shows the coupling conditions for all realistic semiconducting outer walls of a (6,4) inner tube with an interwall spacing of 0.26−0.41 nm. The electronic bands are perturbed more strongly for small ϑ, φ, and interwall distances.

To study the effect of moiré coupling on the vibrational frequencies, we focus on the radial breathing mode (RBM) with an eigenvector in the radial direction.[12] For SWCNTs the RBM frequency scales with $\sim 1/d$ (where d is the tube diameter),[12] and this has been widely used to study nanotube interactions with various exterior[30−32] and interior[33,34] environments. The moiré coupling changes the total energy of the inner tube by

$$\Delta E(R)_i = \frac{1}{|\boldsymbol{k}_{\parallel}|}\sum_m \int (E_{DW}^i(\boldsymbol{k}) - E_{SW}^i(\boldsymbol{k}))\, d\boldsymbol{k} \tag{3}$$

$E_{DW}^i(\boldsymbol{k})$ is the energy of the moiré coupled inner wall. and $E_{SW}^i(\boldsymbol{k})$ is the energy of the SWCNT. $|\boldsymbol{k}_{\parallel}| = 2\pi/|T|$ is the wave vector along the tube axis, with $\boldsymbol{T}$ being the translational symmetry of the nanotube.[12] The integration is performed for $\boldsymbol{k} \in (0,\boldsymbol{k}_{\parallel})$, and the summation runs over the occupied electronic states. The change in the total energy results in the effective force field $F(R)_i = (-\partial\Delta E_i)/\partial R$ experienced by the inner tube. We describe the RBM as a harmonic oscillator with frequency $\omega_{SW} = \sqrt{Q_{SW}/M}$ defined by an effective spring constant Q_{SW} and oscillator mass M. The force $F(R)_i$ is expanded in a Taylor series over a new equilibrium position R_0, $F(R_0)_i + \frac{\partial F(R_0)}{\partial R}(R - R_0) + O(R^2)$, and the equation of motion reads

$$M\ddot{R} = -Q_{SW}(R - R_0) + \frac{\partial F(R_0)}{\partial R}(R - R_0) \tag{4}$$

Equation 4 implies a new effective spring constant $Q_{DW} = Q_{SW} - \frac{\partial F(R_0)}{\partial R}$ that determines the moiré coupled vibrational frequency $\omega_{DW} = \sqrt{Q_{DW}/M}$ and the approximate shift:

$$\Delta\omega = \omega_{DW} - \omega_{SW} \approx \frac{1}{2M\omega_{SW}}\frac{\partial F(R_0)}{\partial R} \tag{5}$$

The force derivative determines the sign of the phonon frequency change. A decrease in the optical transition energies increases the RBM frequencies, whereas an increase corre sponds to smaller RBM frequencies. To obtain a relation between the change in jth transition energy $\Delta E_{jj} = E_{jj}^{DW} - E_{jj}^{SW}$ and the RBM shift $\Delta\omega$, we write the coupling amplitude as $u_0(R) = \gamma_0 e^{R/\lambda + c}$, where γ_0 = 8.1 eV, λ = 0.41 Å, and c = 4.2.[7,9] From eq 5 we find

$$\Delta\omega = \frac{2\sum_m A_m}{mB_j}\frac{\Delta E_{ii}}{M\lambda^2\omega_{SW}} \approx \alpha_j \Delta E_{jj} \tag{6}$$

M refers to the mass of two carbon atoms, A_m corresponds to the fraction of energy change in the mth electron state, B_j reflects the band gap variation of the jth optical transition, and overall a_j contains inner wall specific parameters (see the Supporting Information for details). Equation 6 predicts a linear relation between the transition energy and frequency shifts in radial phonons such as the RBM; we now can experimentally verify this prediction.

We use resonance Raman spectroscopy to find the RBM frequencies of DWCNTs and their corresponding transition energies E_{22}.[12,33,35] The Raman spectra of S@S DWCNTs contain RBM peaks of the inner walls for frequencies above 200 cm^{-1} and RBMs of the outer walls for smaller frequencies (Figure 2a). Characteristically, the RBM peaks of a nanotube split into several components when the tube is the inner part of a DWCNT, as we show for the example of a (7,5) nanotube in Figure 2b,c. By a change in the excitation energy (Figure 2a), different tubes get in and out of resonance, which we will use to assign the chiral indices (n_1^i,n_2^i) of inner walls.[35,36] Generally, the RBM peaks from different combinations of inner and outer walls overlap. We therefore start our analysis with the (6,4) inner wall, because its RBM is well separated from the other peaks (Figure 2a). We collect the Raman spectra at 15 wavelengths across the (6,4) E_{22} resonance (see exemplary spectra in Figure 3a). The peak appears to shift in frequency with laser energy, but this impression is incorrect; instead the RBM region contains at least six different components with constant frequencies between 332 and 347 cm^{-1}. The varying distribution between intensities leads to the impression of an overall frequency shift. Each component corresponds to at least one DWCNT. The frequency of the (6,4) SWCNT ($RBM_{(6,4)}$ = 333 cm^{-1}, vertical line) increased by up to 14 cm^{-1} or almost 5% in the DWCNTs.

The resonance energies of the inner tube E_{22} also differ with varying RBM frequency (Figure 3a). The intensity distribution

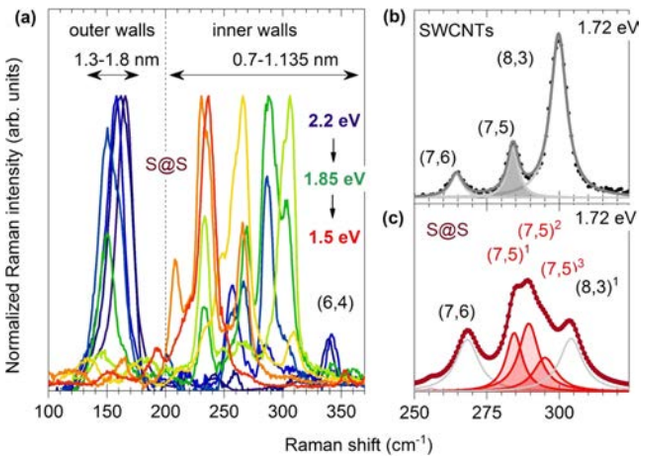

Figure 2. (a) Resonance Raman spectra of S@S in the region of RBMs, excited between 1.5 and 2 eV. (b) RBM spectrum of SWCNTs, with the (7,5) peak highlighted. (c) Raman spectrum of the S@S DWCNTs with (7,5)@(n_1^o,n_2^o) peaks highlighted.

between the modes depends on the excitation energy; at 2.1 eV the low frequency modes were resonant, whereas at 1.9 eV the high frequency modes were the strongest. We quantified the changes in E_{22} by resonance Raman scattering using fully tunable lasers.[33,37,38] Each (6,4)@(n_1^o,n_2^o) component had a different transition energy E_{22} (Figure 3b,c). The shift in resonance between the DWCNTs and SWCNTs, ΔE_{22} = 20−200 meV, increased linearly with the change in RBM frequency, as shown in Figure 3d, with the slope of the line α_2 = −94 cm^{-1}/eV. The experimental data thus fully agree with the predictions of eq 6. We note that ΔE_{22} remains finite at the zero RBM shift. This offset is due to the dielectric effect, because the outer wall induces higher screening in comparison to an uncovered SWCNT. The dielectric red shift of ∼35 meV lies within theoretical predictions.[39]

Equation 6 was used to perform a full assignment of the DWCNTs under investigation and to identify the host chiralities for the (6,4) inner wall. We performed band structure calculations for all possible hosts by eq 1, the same as we did in Figure 1d, and calculated the theoretical band gaps E_{22}^{DW}. The differences $\Delta E_{22} = E_{22}^{DW} - E_{22}^{SW}$ are plotted as a function of diameter spacing in Figure 4. This simulation is for DWCNTs of identical inner and outer handedness that appear to grow preferentially.[40] In Figure S3 in the Supporting Information we show the additional shift for opposite handedness. In most cases it is very small, but, for example, the (6,4)@(8,13) tube has an additional shift $\Delta E_{22} \approx -20$ meV in comparison to the (6,4)@(13,8) tube. The horizontal lines show the experimental data, where overlap with theoretical predictions identifies the host chirality. This way the RBM at 346.5 cm^{-1} was assigned to the (6,4)@(12,8) tube, 343.3 cm^{-1} to the (6,4)@(17,0) tube, 341 cm^{-1} to the (6,4)@(16,2) tube, and 338.9 cm^{-1} to the (6,4)@(15,4) tube. The RBM peak at 335.5 cm^{-1} originates from several species, including (6,4)@(17,1), (6,4)@(16,3), (6,4)@(14,6), (6,4)@(13,8), and (6,4)@(15,5) tubes, and the RBM at 332 cm^{-1} can be attributed to the (6,4)@(18,1), (6,4)@(14,7), and (6,4)@(17,3) nanotubes. The right axis represents the vibrational moiré shift, obtained using the experimental α_2

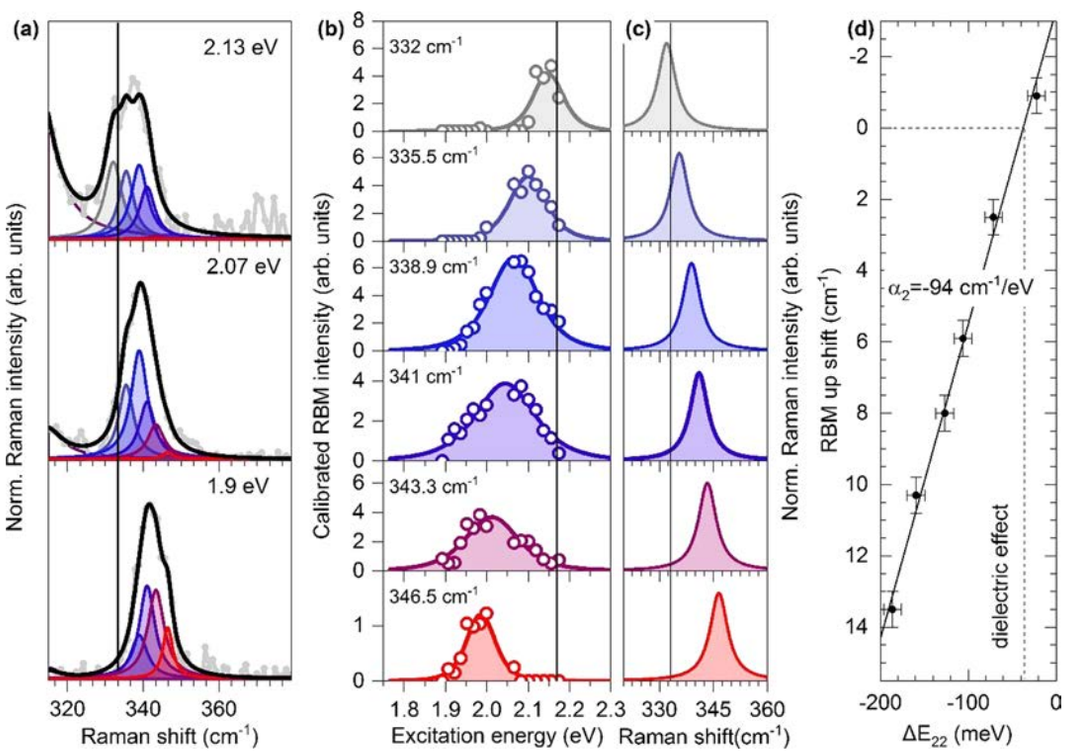

Figure 3. Resonance Raman spectroscopy of (6,4)@(n_1^o,n_2^o) DWCNTs. (a) Spectral composition of exemplary Raman spectra excited at 2.13, 2.07, and 1.9 eV (from top to bottom). The peak color highlights the different outer tubes. (b) Raman resonance profiles of the RBMs shown in (c), where the integrated peak area is plotted versus excitation energy. The solid vertical line corresponds to the E_{22} transition of the (6,4) SWCNT. Vertical lines in (a) and (c) correspond to the RBM of the SWCNT. (d) Difference between the (6,4)@(n_1^o,n_2^o) and (6,4) RBM frequencies vs the red shift of the E_{22} transition in DWCNTs in comparison to the (6,4) SWCNT.

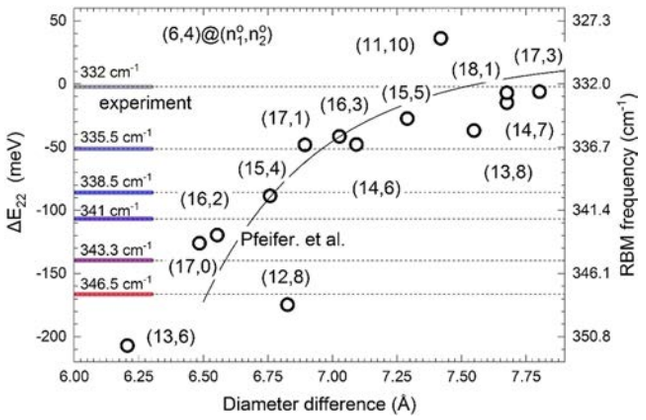

Figure 4. Electromechanical coupling in $(6,4)@(n_1^o,n_2^o)$ DWCNTs. The symbols show the E_{22} shift calculated with eq 1 in comparison to the SWCNT: namely, $\Delta E_{22} = E_{22}^{DW} - E_{22}^{SW}$ versus the diameter difference between the walls. Horizontal lines show experimental data deduced from resonance Raman profiles shifted by dielectric screening (35 meV). The right axis stands for vibrational coupling: i.e., the RBM shift obtained with eq 6 and $\alpha_2 = -93.8$ cm^{-1}/eV. The solid line shows the model of Pfeiffer et al.[44] (see eq S6 in the Supporting Information).

value. In such a manner one can predict the RBM frequency and transition energy of any possible $(6,4)@(n_1^o,n_2^o)$ chiral combination.

We performed an analysis similar to that for the (6,4) inner tube for the eight other inner nanotube species. For these inner walls the RBMs sometimes overlap, as shown in Figure 2c. We were able to decompose them experimentally using eq 6 under the constraint of using the minimum number of components with constant frequencies. Each fitted peak showed a linear relation between the RBMs and E_{22} shifts, as already observed for the (6,4) species. We show in Figure 5a,b two examples of resonance Raman profiles for $(7,5)@(n_1^o,n_2^o)$ and $(9,4)@(n_1^o,n_2^o)$ nanotubes. We determined the vibrational and transition energies for each subpeak. Figure 5c shows a Kataura plot of DWCNTs (closed symbols) and SWCNTs (open): i.e., a plot of E_{22} versus ω_{RBM}. For each SWCNT inner wall the corresponding series of DWCNTs form a line on the Kataura plot. This plot can be used to identify chiral indices and coupling strengths via Raman scattering. The E_{22} transition energies of most DWCNTs are smaller than in the corresponding SWCNTs even for little or no shift of the RBMs. As shown in Figure 3e, we attribute this offset to the dielectric screening of the inner tube by the outer species.[41] The dielectric shift varies between 35 meV in $(6,4)@(n_1^o,n_2^o)$ and 55 meV in $(8,3)@(n_1^o,n_2^o)$ DWCNTs (Figure 5c). This variation can be explained by a diameter dependence of the self screening effect.[39] As the tube diameter increases, a larger fraction of the exciton wave function extends to the outside, resulting in a higher sensitivity to environmental effects.[39]

The changes in RBM and E_{22} energies are both proportional to the moiré coupling strength. Moiré systems reach strong coupling if the shift of the transition energy ΔE_{22} is larger than its decay rate γ. Since the coupling affects both electronic and vibrational states, the shift in RBM frequency can be used to identify strong coupling. The typical full width at half maximum (fwhm) at room temperature is determined from the resonance Raman profiles as $\gamma = 75$ meV. With the experimental α_2 value we conclude that $\Delta\omega \approx 5$ cm^{-1} signals

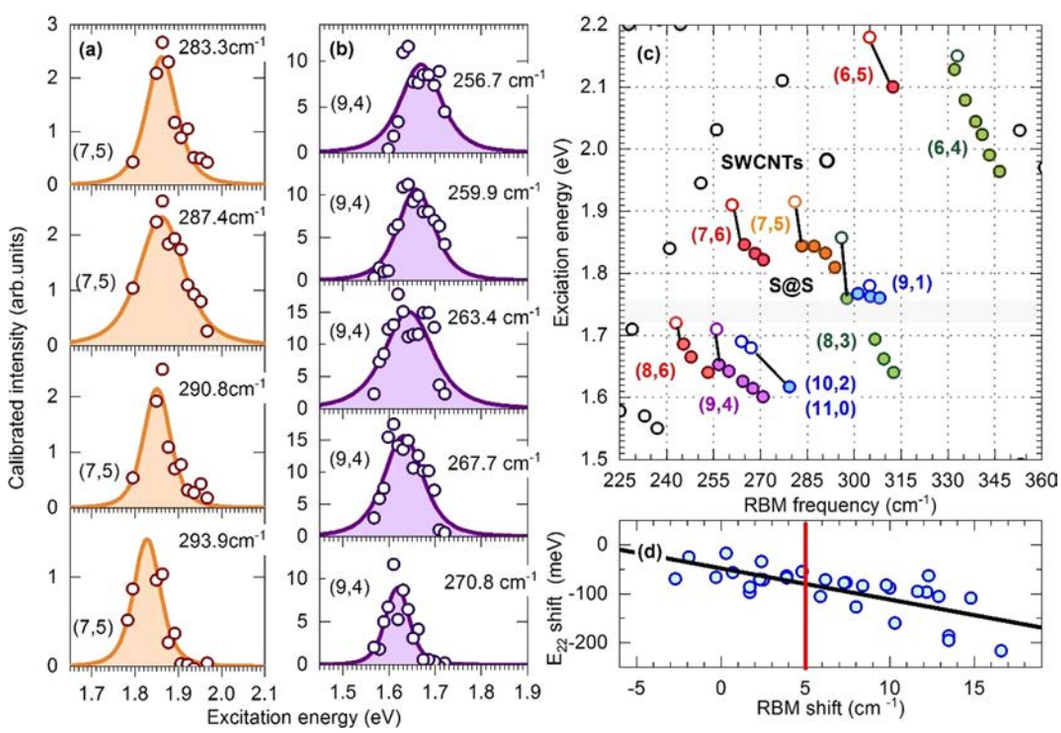

Figure 5. Mechanical coupling in small diameter DWCNTs. Resonance Raman profiles of (a) $(7,5)@(n_1^o,n_2^o)$ and (b) $(9,4)@(n_1^o,n_2^o)$. The symbols show the experimental data, and the lines are the fits. (c) Kataura plot for the S@S sample (filled circles) with transition energy E_{22} plotted vs RBM frequency. SWCNTs[33] are shown by open circles, and different colors were used to separate different inner walls. The values are given in Table S1 in the Supporting Information. The gray line marks the wavelength range that is inaccessible in our setup. (d) Scattering plot for the E_{22} and RBM shifts. The red line divides strongly and weakly coupled DWCNTs.

strong coupling. The red line in Figure 5d divides strongly and weakly coupled DWCNTs. The majority of the DWCNTs in the S@S sample are in the strong coupling regime.

In the strong coupling regime, the electronic states shift by up to 10% to smaller energies. This regime is particularly interesting for optical studies such as interwall energy transfer, interwall optical excitations, and inelastic scattering. To find such a tube system, one should aim for DWCNTs with a large shift of the RBM frequency in comparison to that of the SWCNT. This will simplify the search for the moire coupled structures; up to now one required transmission electron microscopy to find strongly moiré coupled DWCNTs, such as (12,11)@(17,16) found by Zhao et al.[9] The second types of DWCNTs are tubes with flat bands that were predicted for $\varphi \approx 0$ and $\vartheta \approx \frac{\pi}{6}$.[7] These tubes are expected to show peculiar transport phenomena such as phase transitions between insulating and superconducting states. Switching between the phases could be exploited for perfect field effect transistors. Examples of such tubes in the small diameter regime are (9,1) @(n_1°,n_2°) and (11,0)@(n_1°,n_2°) (see the blue symbols in Figure 5c). Finally, there is the third weakly interacting case with a polycrystalline intratube pattern (large φ and ϑ) and large interlayer distance (see Figure 1c). These DWCNTs are suitable for environmental shielding and sheathing in electrical applications.[42] The interaction between the walls is expected to be very weak, which may be the reason for the blocked energy transfer between the walls in such DWCNTs.[43]

We have presented a new model for the RBM shifts in DWCNTs accounting for crystallographic orientations and interlayer distances. The previous model by Pfeiffer et al.[21,28] only contained the dependence on the intralayer spacing and is insufficient to reproduce all experimentally observed shifts. We compared our data with the previous model in Figure 4. Stronger deviations are found for DWCNTs with strong coupling (φ and ϑ are close to zero). A good example is the (6,4)@(12,8) nanotube, where we predict a RBM frequency of 346.5 cm^{-1} as opposed to 339 cm^{-1} from previous works.[21,44] Further examples that we assigned differently are (6,4) @(11,10), (6,4)@(13,8), and (6,4)@(14,8). In the weak coupling regime both models seem to deliver similar results; however, the underlying model of Pfeiffer et al.[21,28] is not compatible with the optical energy shifts. The suggested effective pressure should introduce a strain induced transition energy shift in opposite directions for different $mod(3,n_1^\circ,n_2^\circ)$ types of inner walls.[45] In contrast, we find the same shift direction for (7,5)@(n_1°,n_2°) and (7,6)@(n_1°,n_2°) (see Figure 5c). Therefore, only the moiré model can reproduce the RBM and transition energy shifts, in both weakly and strongly coupled DWCNTs. The correct RBM shift position is required for an identification of the chiral indices, which is critical for understanding the physics effects in DWCNTs and their derivatives.

Moiré coupling also affects vibrational frequencies in more complex one dimensional heterostructures such as DWCNTs with encapsulated carbon chains.[46] The chirality of the inner nanotube was shown to influence the vibrational frequency of the chain.[47] This statement can be expanded upon using our chiral assignment of DWCNTs, where the RBM at 335 cm^{-1} belongs to a weakly coupled (6,4)@(n_1°,n_2°) and not to a (6,5) @(n_1°,n_2°).[47] This DWCNT is in the weak coupling regime and corresponds to the 1830.5 cm^{-1} frequency of the encapsulated carbon chain. The same (6,4) inner wall, but in the strong coupling regime (RBM = 348 cm^{-1}), contains a chain with frequency ~1800 cm^{-1}. This large 30 cm^{-1} discrepancy shows that the chirality of the outer wall influences the vibrational frequency of the encapsulated carbon chain. It would be extremely interesting to study the transition energies of the carbon chains and their DWCNT hosts using multiwavelength resonance Raman scattering.

In conclusion, we have shown how moiré coupling affects the vibrations and the electronic transitions of DWCNTs. The transition energy shifts to a smaller energy, and the RBM frequencies increase for a smaller interlayer spacing and aligned chiral vectors, as predicted in two moiré coupled graphene cylinders. The linear correlation between the vibrational and optical shifts is explained by a macroscopic theory, treating the RBMs as two oscillators coupled via the moiré potential. We demonstrated a strong effect of moiré coupling on the vibrational states, which will assess electronic coupling in the one dimensional twisted hetero and homostructures. Our experiments show that DWCNTs are more than the simple sum of two SWCNTs and need to be treated as novel materials.

AUTHOR INFORMATION

Corresponding Author

Georgy Gordeev − *Department of Physics, Freie Universität Berlin, 14195 Berlin, Germany;* ; Email: gordeev@zedat.fu berlin.de

Authors

Sören Wasserroth − *Department of Physics, Freie Universität Berlin, 14195 Berlin, Germany; Fritz Haber Institut der Max Planck Gesellschaft, 14195 Berlin, Germany*

Han Li − *Institute of Nanotechnology, Karlsruhe Institute of Technology, Karlsruhe, Germany*

Benjamin Flavel − *Institute of Nanotechnology, Karlsruhe Institute of Technology, Karlsruhe, Germany;*

Stephanie Reich − *Department of Physics, Freie Universität Berlin, 14195 Berlin, Germany;*

Notes

The authors declare no competing financial interest.

ACKNOWLEDGMENTS

This work was supported by the Focus Area NanoScale of Freie Universitaet Berlin. S.R. acknowledges support by the Deutsche Forschungsgemeinschaft under SPP 2244.

REFERENCES

(1) Gustafsson, M. G. L. Surpassing the Lateral Resolution Limit by a Factor of Two Using Structured Illumination Microscopy. *J. Microsc.* **2000**, *198* (2), 82−87.

(2) Cao, Y.; Fatemi, V.; Fang, S.; Watanabe, K.; Taniguchi, T.; Kaxiras, E.; Jarillo Herrero, P. Unconventional Superconductivity in Magic Angle Graphene Superlattices. *Nature* **2018**, *556* (7699), 43−50.

(3) Li, G.; Luican, A.; Lopes Dos Santos, J. M. B.; Castro Neto, A. H.; Reina, A.; Kong, J.; Andrei, E. Y. Observation of Van Hove Singularities in Twisted Graphene Layers. *Nat. Phys.* **2010**, *6* (2), 109−113.

(4) Weston, A.; Zou, Y.; Enaldiev, V.; Summerfield, A.; Clark, N.; Zólyomi, V.; Graham, A.; Yelgel, C.; Magorrian, S.; Zhou, M.; Zultak, J.; Hopkinson, D.; Barinov, A.; Bointon, T. H.; Kretinin, A.; Wilson, N. R.; Beton, P. H.; Fal'ko, V. I.; Haigh, S. J.; Gorbachev, R. Atomic Reconstruction in Twisted Bilayers of Transition Metal Dichalcogenides. *Nat. Nanotechnol.* **2020**, *15* (7), 592−597.

(5) Tang, Y.; Li, L.; Li, T.; Xu, Y.; Liu, S.; Barmak, K.; Watanabe, K.; Taniguchi, T.; MacDonald, A. H.; Shan, J.; Mak, K. F. Simulation of Hubbard Model Physics in WSe2/WS2Moiré Superlattices. *Nature* **2020**, *579* (7799), 353−358.

(6) Xiang, R.; Inoue, T.; Zheng, Y.; Kumamoto, A.; Qian, Y.; Sato, Y.; Liu, M.; Tang, D.; Gokhale, D.; Guo, J.; Hisama, K.; Yotsumoto, S.; Ogamoto, T.; Arai, H.; Kobayashi, Y.; Zhang, H.; Hou, B.; Anisimov, A.; Maruyama, M.; Miyata, Y.; Okada, S.; Chiashi, S.; Li, Y.; Kong, J.; Kauppinen, E. I.; Ikuhara, Y.; Suenaga, K.; Maruyama, S. One Dimensional van Der Waals Heterostructures. *Science (Washington, DC, U. S.)* **2020**, *367* (6477), 537−542.

(7) Koshino, M.; Moon, P.; Son, Y. W. Incommensurate Double Walled Carbon Nanotubes as One Dimensional Moiré Crystals. *Phys. Rev. B: Condens. Matter Mater. Phys.* **2015**, *91* (3), 035405.

(8) Liu, K.; Jin, C.; Hong, X.; Kim, J.; Zettl, A.; Wang, E.; Wang, F. Van Der Waals Coupled Electronic States in Incommensurate Double Walled Carbon Nanotubes. *Nat. Phys.* **2014**, *10* (10), 737−742.

(9) Zhao, S.; Moon, P.; Miyauchi, Y.; Nishihara, T.; Matsuda, K.; Koshino, M.; Kitaura, R. Observation of Drastic Electronic Structure Change in a One Dimensional Moiré Superlattice. *Phys. Rev. Lett.* **2020**, *124* (10), 106101.

(10) Gallagher, M. J.; Chen, D.; Jacobsen, B. P.; Sarid, D.; Lamb, L. D.; Tinker, F. A.; Jiao, J.; Huffman, D. R.; Seraphin, S.; Zhou, D. Characterization of Carbon Nanotubes by Scanning Probe Microscopy. *Surf. Sci. Lett.* **1993**, *281* (3), 335−340.

(11) Reich, S.; Thomsen, C.; Maultzsch, J. *Carbon Nanotubes: Basic Concepts and Physical Properties*; Wiley VCH: 2004.

(12) Thomsen, C.; Reich, S. Raman Scattering in Carbon Nanotubes. In *Light Scattering in Solids IX*; Manuel, C., Merlin, R., Eds.; Springer: 2007; pp 164−169.

(13) Liu, K.; Wang, W.; Xu, Z.; Bai, X.; Wang, E.; Yao, Y.; Zhang, J.; Liu, Z. Chirality Dependent Transport Properties of Double Walled Nanotubes Measured in Situ on Their Field Effect Transistors. *J. Am. Chem. Soc.* **2009**, *131* (1), 62−63.

(14) Zhao, S.; Moon, P.; Miyauchi, Y.; Nishihara, T.; Matsuda, K.; Koshino, M.; Kitaura, R. Observation of Drastic Electronic Structure Change in a One Dimensional Moiré Superlattice. *Phys. Rev. Lett.* **2020**, *124* (10), 106101.

(15) Liu, K.; Hong, X.; Wu, M.; Xiao, F.; Wang, W.; Bai, X.; Ager, J. W.; Aloni, S.; Zettl, A.; Wang, E.; Wang, F. Quantum Coupled Radial Breathing Oscillations in Double Walled Carbon Nanotubes. *Nat. Commun.* **2013**, *4*, 1375.

(16) Li, H.; Gordeev, G.; Wasserrot, S.; Chakravadhanula, V. S. K.; Neelakandhan, S. K. C.; Hennrich, F.; Jorio, A.; Reich, S.; Krupke, R.; Flavel, B. S. Inner and Outer Wall Sorting of Double Walled Carbon Nanotubes. *Nat. Nanotechnol.* **2017**, *12* (12), 1176−1182.

(17) Moore, K. E.; Pfohl, M.; Tune, D. D.; Hennrich, F.; Dehm, S.; Chakradhanula, V. S. K.; Kübel, C.; Krupke, R.; Flavel, B. S. Sorting of Double Walled Carbon Nanotubes According to Their Outer Wall Electronic Type via a Gel Permeation Method. *ACS Nano* **2015**, *9* (4), 3849−3857.

(18) Moore, K. E.; Pfohl, M.; Hennrich, F.; Chakradhanula, V. S. K.; Kuebel, C.; Kappes, M. M.; Shapter, J. G.; Krupke, R.; Flavel, B. S. Separation of Double Walled Carbon Nanotubes by Size Exclusion Column Chromatography. *ACS Nano* **2014**, *8* (7), 6756−6764.

(19) Eliel, G. S. N.; Moutinho, M. V. O.; Gadelha, A. C.; Righi, A.; Campos, L. C.; Ribeiro, H. B.; Chiu, P. W.; Watanabe, K.; Taniguchi, T.; Puech, P.; Paillet, M.; Michel, T.; Venezuela, P.; Pimenta, M. A. Intralayer and Interlayer Electron Phonon Interactions in Twisted Graphene Heterostructures. *Nat. Commun.* **2018**, *9* (1), 1221.

(20) Lui, C. H.; Ye, Z.; Ji, C.; Chiu, K. C.; Chou, C. T.; Andersen, T. I.; Means Shively, C.; Anderson, H.; Wu, J. M.; Kidd, T.; Lee, Y. H.; He, R. Observation of Interlayer Phonon Modes in van Der Waals Heterostructures. *Phys. Rev. B: Condens. Matter Mater. Phys.* **2015**, *91* (16), 1−7.

(21) Pfeiffer, R.; Simon, F.; Kuzmany, H.; Popov, V. N. Fine Structure of the Radial Breathing Mode of Double Wall Carbon Nanotubes. *Phys. Rev. B: Condens. Matter Mater. Phys.* **2005**, *72* (16), 161404.

(22) Pfeiffer, R.; Simon, F.; Kuzmany, H.; Popov, V. N.; Zólyomi, V.; Kürti, J. Tube Tube Interaction in Double Wall Carbon Nanotubes. *Phys. Status Solidi B* **2006**, *243* (13), 3268−3272.

(23) Villalpando Paez, F.; Muramatsu, H.; Kim, Y. A.; Farhat, H.; Endo, M.; Terrones, M.; Dresselhaus, M. S. Wall to Wall Stress Induced in (6,5) Semiconducting Nanotubes by Encapsulation in Metallic Outer Tubes of Different Diameters: A Resonance Raman Study of Individual C60 Derived Double Wall Carbon Nanotubes. *Nanoscale* **2010**, *2* (3), 406−411.

(24) Villalpando Paez, F.; Moura, L. G.; Fantini, C.; Muramatsu, H.; Hayashi, T.; Kim, Y. A.; Endo, M.; Terrones, M.; Pimenta, M. A.; Dresselhaus, M. S. Tunable Raman Spectroscopy Study of CVD and Peapod Derived Bundled and Individual Double Wall Carbon Nanotubes. *Phys. Rev. B: Condens. Matter Mater. Phys.* **2010**, *82* (15), 1−9.

(25) Levshov, D.; Than, T. X.; Arenal, R.; Popov, V. N.; Parret, R.; Paillet, M.; Jourdain, V.; Zahab, A. A.; Michel, T.; Yuzyuk, Y. I.; Sauvajol, J. L. Experimental Evidence of a Mechanical Coupling between Layers in an Individual Double Walled Carbon Nanotube. *Nano Lett.* **2011**, *11* (11), 4800−4804.

(26) Dobardžić, E.; Maultzsch, J.; Milošević, I.; Thomsen, C.; Damnjanović, M. The Radial Breathing Mode Frequency in Double Walled Carbon Nanotubes: An Analytical Approximation. *Phys. Status Solidi Basic Res.* **2003**, *237* (2), R7−R10.

(27) Popov, V. N.; Henrard, L. Breathinglike Phonon Modes of Multiwalled Carbon Nanotubes. *Phys. Rev. B: Condens. Matter Mater. Phys.* **2002**, *65* (23), 2354151−2354156.

(28) Pfeiffer, R.; Kramberger, C.; Simon, F.; Kuzmany, H.; Popov, V. N.; Kataura, H. Interaction between Concentric Tubes in DWCNTs. *Eur. Phys. J. B* **2004**, *42* (3), 345−350.

(29) Reich, S.; Maultzsch, J.; Thomsen, C.; Ordejón, P. Tight Binding Description of Graphene. *Phys. Rev. B: Condens. Matter Mater. Phys.* **2002**, *66* (3), 354121−354125.

(30) Wenseleers, W.; Cambré, S.; Čulin, J.; Bouwen, A.; Goovaerts, E. Effect of Water Filling on the Electronic and Vibrational Resonances of Carbon Nanotubes: Characterizing Tube Opening by Raman Spectroscopy. *Adv. Mater.* **2007**, *19* (17), 2274−2278.

(31) Cambré, S.; Campo, J.; Beirnaert, C.; Verlackt, C.; Cool, P.; Wenseleers, W. Asymmetric Dyes Align inside Carbon Nanotubes to Yield a Large Nonlinear Optical Response. *Nat. Nanotechnol.* **2015**, *10* (3), 248−252.

(32) Li, H.; Gordeev, G.; Garrity, O.; Peyyety, N. A.; Selvasundaram, P. B.; Dehm, S.; Krupke, R.; Cambré, S.; Wenseleers, W.; Reich, S.; Zheng, M.; Fagan, J. A.; Flavel, B. S. Separation of Specific Single Enantiomer Single Wall Carbon Nanotubes in the Large Diameter Regime. *ACS Nano* **2020**, *14* (1), 948−963.

(33) Maultzsch, J.; Telg, H.; Reich, S.; Thomsen, C. Radial Breathing Mode of Single Walled Carbon Nanotubes: Optical

Transition Energies and Chiral Index Assignment. *Phys. Rev. B: Condens. Matter Mater. Phys.* **2005**, *72* (20), 205438.
(34) Araujo, P. T.; Jorio, A.; Dresselhaus, M. S.; Sato, K.; Saito, R. Diameter Dependence of the Dielectric Constant for the Excitonic Transition Energy of Single Wall Carbon Nanotubes. *Phys. Rev. Lett.* **2009**, *103* (14), 1−4.
(35) Telg, H.; Maultzsch, J.; Reich, S.; Hennrich, F.; Thomsen, C. Chirality Distribution and Transition Energies of Carbon Nanotubes. *Phys. Rev. Lett.* **2004**, *93* (17), 1−4.
(36) Fantini, C.; Jorio, A.; Souza, M.; Strano, M. S.; Dresselhaus, M. S.; Pimenta, M. A. Optical Transition Energies for Carbon Nanotubes from Resonant Raman Spectroscopy: Environment and Temperature Effects. *Phys. Rev. Lett.* **2004**, *93* (14), 147406.
(37) Telg, H.; Maultzsch, J.; Reich, S.; Thomsen, C. Resonant Raman Intensities and Transition Energies of the E11 Transition in Carbon Nanotubes. *Phys. Rev. B: Condens. Matter Mater. Phys.* **2006**, *74* (11), 115415.
(38) Gordeev, G.; Jorio, A.; Kusch, P.; Vieira, B. G. M.; Flavel, B.; Krupke, R.; Barros, E. B.; Reich, S. Resonant Anti Stokes Raman Scattering in Single Walled Carbon Nanotubes. *Phys. Rev. B: Condens. Matter Mater. Phys.* **2017**, *96* (24), 245415.
(39) Tomio, Y.; Suzuura, H.; Ando, T. Interwall Screening and Excitons in Double Wall Carbon Nanotubes. *Phys. Rev. B: Condens. Matter Mater. Phys.* **2012**, *85* (8), 37−39.
(40) Liu, Z.; Suenaga, K.; Yoshida, H.; Sugai, T.; Shinohara, H.; Iijima, S. Determination of Optical Isomers for Left Handed or Right Handed Chiral Double Wall Carbon Nanotubes. *Phys. Rev. Lett.* **2005**, *95* (18), 1−4.
(41) Walsh, A. G.; Vamivakas, A. N.; Yin, Y.; Cronin, S. B.; Ünlü, M. S.; Goldberg, B. B.; Swan, A. K. Screening of Excitons in Single, Suspended Carbon Nanotubes. *Nano Lett.* **2007**, *7* (6), 1485−1488.
(42) Nakar, D.; Gordeev, G.; MacHado, L. D.; Popovitz Biro, R.; Rechav, K.; Oliveira, E. F.; Kusch, P.; Jorio, A.; Galvaõ, D. S.; Reich, S.; Joselevich, E. Few Wall Carbon Nanotube Coils. *Nano Lett.* **2020**, *20* (2), 953−962.
(43) Levshov, D. I.; Parret, R.; Tran, H. N.; Michel, T.; Cao, T. T.; Nguyen, V. C.; Arenal, R.; Popov, V. N.; Rochal, S. B.; Sauvajol, J. L.; Zahab, A. A.; Paillet, M. Photoluminescence from an Individual Double Walled Carbon Nanotube. *Phys. Rev. B: Condens. Matter Mater. Phys.* **2017**, *96* (19), 1−7.
(44) Pfeiffer, R.; Peterlik, H.; Kuzmany, H.; Simon, F.; Pressl, K.; Knoll, P.; Rümmeli, M. H.; Shiozawa, H.; Muramatsu, H.; Kim, Y. A.; Hayashi, T.; Endo, M. A Detailed Comparison of CVD Grown and Precursor Based DWCNTs. *Phys. Status Solidi B* **2008**, *245* (10), 1943−1946.
(45) Huang, M.; Wu, Y.; Chandra, B.; Yan, H.; Shan, Y.; Heinz, T. F.; Hone, J. Direct Measurement of Strain Induced Changes in the Band Structure of Carbon Nanotubes. *Phys. Rev. Lett.* **2008**, *100* (13), 136803.
(46) Shi, L.; Rohringer, P.; Suenaga, K.; Niimi, Y.; Kotakoski, J.; Meyer, J. C.; Peterlik, H.; Wanko, M.; Cahangirov, S.; Rubio, A.; Lapin, Z. J.; Novotny, L.; Ayala, P.; Pichler, T. Confined Linear Carbon Chains as a Route to Bulk Carbyne. *Nat. Mater.* **2016**, *15* (6), 634−639.
(47) Heeg, S.; Shi, L.; Poulikakos, L. V.; Pichler, T.; Novotny, L. Carbon Nanotube Chirality Determines Properties of Encapsulated Linear Carbon Chain. *Nano Lett.* **2018**, *18* (9), 5426−5431.